scientific reports

Check for updates

OPEN

$Cs_2AgBiBr_6$ and related Halide double perovskite porous single crystals

Maurya Sandeep Pradeepkumar[1,2], Aruchamy Kathirvel[1,2], Sayan Ghosh[1] & Chandran Sudakar[1]✉

The utilization of single crystals is exponentially growing in optoelectronic devices due to their exceptional benefits, including high phase purity and the absence of grain boundaries. However, achieving single crystals with a porous structure poses significant challenges. In this study, we present a method for fabricating porous single crystals (porous-SC) of $Cs_2AgBiBr_6$ and related halide double perovskites using an infrared-assisted spin coating technique. The porous-SC are formed through a non-classical crystallization process, where oriented crystallographic platelets assemble into porous-SC clusters and merge to create iso-oriented single crystalline building blocks, with pore regions primarily located in the gaps between the platelets. Large porous square-shaped $Cs_2AgBiBr_6$ halide double perovskite (HDP) single crystals with lateral dimension ~ 10 to 50 µm and few µm thickness are realized with preferred orientation along {*h00*} on the FTO substrate upon subsequent spin-coating of layers. Analysis using angle-resolved polarized Raman spectroscopy, X-ray diffraction and transmission electron microscopy confirms the formation of single crystals of $Cs_2AgBiBr_6$. Further, to get a uniform coating of highly interconnected porous-SC clusters, wiping method under IR illumination is employed. Solar cell devices fabricated from these porous-SCs perform better with J_{SC} =1.40 mA/cm^2, V_{OC}=1.04 V and η = 0.86% than the conventional polycrystalline thin films with J_{SC} = 0.55 mA/cm^2, V_{OC}=0.94 V and η = 0.28%. $Cs_2AgBiBr_6$ porous-SC shows potential for a wide range of optoelectronic and photoelectrochemical applications.

Keywords Halide double perovskite, $Cs_2AgBiBr_6$, Porous, Single crystal, Solar cell

Porous single crystals (porous-SCs) offer a unique combination of the advantages found in both the porous materials and the grain boundary-free single crystals[1,2]. Developing porous-SCs holds the promise of providing increased surface area and exposing various crystallographic facets with distinct surface energies, thereby facilitating the formation of coherent interfaces in devices. In the past, porous-SCs of oxides like TiO_2 were reported as a solution to challenges associated with electron transport across interfaces, a common issue encountered in nanoparticle systems[3]. However, the growth of such porous-SCs was mostly achievable through the seeding of the silica bead templates. There are also examples of porous single crystals (TiO_2, TiN, CeO_2, VN, Mo_2N) and porous microstructures for other oxides and nitrides[3–7] with sizes mostly in µm to mm range. So far, there are no reports on growing halide perovskite porous-SCs directly from the solution.

In recent years, halide perovskites have emerged as extensively researched materials with applications spanning photovoltaics[8], photodetectors[9], photoelectrochemical devices[10], and sensors[11]. Developing methods for producing porous-SCs of halide perovskites holds significant promise. Specifically, the fabrication of porous-SCs of $Cs_2AgBiBr_6$ halide double perovskite (HDP) is of particular interest due to its Pb-free composition, suitable band gap (indirect~1.8 eV & direct ~ 2.2 eV)[12,13], favorable carrier effective mass (0.1 to 0.4 m_e)[14], and prolonged carrier lifetimes (> 1 µs)[15]. HDP porous-SCs will be a viable option for various device applications.

We present a simple approach utilizing spin coating combined with infrared (IR) light exposure to create porous-SCs of $Cs_2AgBiBr_6$ and related HDPs. The porous structure is a result of the rapid growth of single crystalline faceted nanoplatelets organized in a stack-of-cards-like microstructure on the substrate plane. To underscore the significance of porous-SCs for device applications, we assess the performance of photovoltaic and photodetector devices in comparison to the devices fabricated with non-porous thin films of $Cs_2AgBiBr_6$ with the identical composition obtained without IR lamp exposure.

[1]Multifunctional Materials Laboratory, Department of Physics, Indian Institute of Technology Madras, Chennai 600036, India. [2]Maurya Sandeep Pradeepkumar and A. Kathirvel contributed equally to this work. ✉email: csudakar@iitm.ac.in

Experimental procedure

Porous single-crystalline $Cs_2AgBiBr_6$ crystals are synthesized following the procedure outlined in Fig. 1(a). Initially, a precursor solution for spin coating is prepared by mixing the metal halides as detailed in the experimental section provided in the supplementary material (step I in Fig. 1a). Subsequently, 30 µL of the precursor solution is spin-coated onto a preheated (80 ℃) substrate (such as glass, FTO/glass or m-TiO_2 coated FTO/glass) at 4000 rpm for 45 s (step II in Fig. 1a). Most importantly, during the spin coating process, the substrate is concurrently illuminated with an IR lamp (150 W) positioned at an optimized distance, ensuring that substrate temperature remains ~ 60 to 80 ℃, thereby facilitating rapid solvent evaporation. After coating, the substrate is heated to 80 ℃ for 5 min (step III). Substrates are coated with either a single layer or multiple layers (step IV) and morphological changes are observed for each layer coating. For comparative analysis, films are also spin-coated without exposure to an IR lamp. The $Cs_2AgBiBr_6$ films coated with and without IR exposure are designated as CABB-*w*IR and CABB-*w/o*IR, respectively.

Results and discussion

The X-ray diffraction (XRD) patterns of CABB-*w*IR and CABB-*w/o*IR films (Fig. 1b) reveal the presence of phase pure $Cs_2AgBiBr_6$ HDP, consistent with the ICDD pattern (01-084-8699) representing a cubic elpasolite structure with space group $Fm\bar{3}m$. Notably, these patterns exhibit the absence of any traces of other potential secondary phases such as $Cs_3Bi_2Br_9$, AgBr, and BiBrO. Initially, a polycrystalline pattern is observed for a single-layer coating for CABB-*w*IR (Fig. S1). However, upon coating few layers, the films begin to display intense (200) and (400) diffraction peaks, indicating a pronounced preferred orientation growth along the (*h*00) planes shown in Fig. 1b. The full-width-at-half-maximum of these (200) and (400) diffraction peaks measure 0.116° and

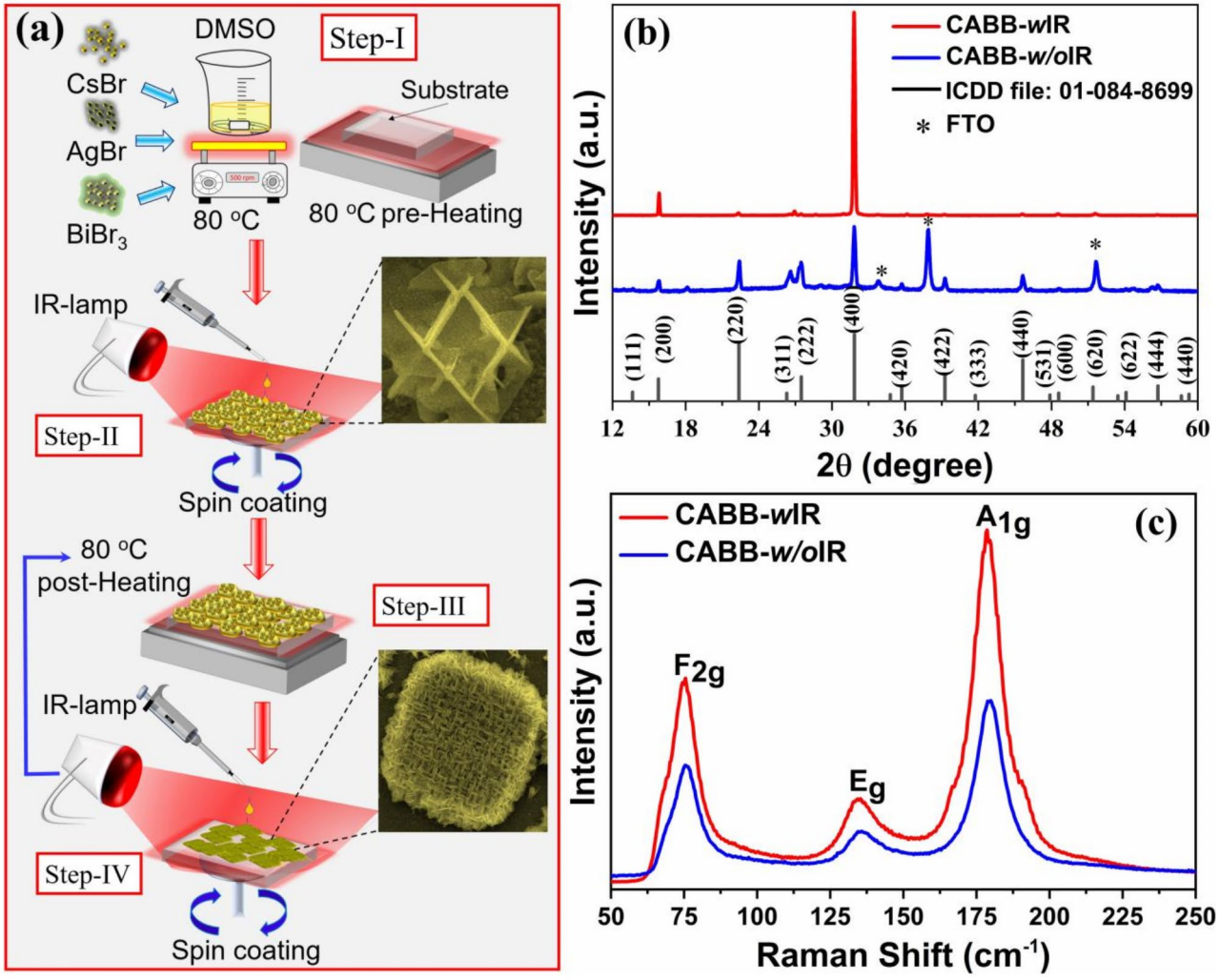

Fig. 1. (**a**) Illustration depicting the fabrication process of porous-SC $Cs_2AgBiBr_6$ HDP (refer to the supplementary file for processing details). (**b**) XRD pattern and (**c**) Raman spectra of $Cs_2AgBiBr_6$ HDP thin films grown without (CABB-*w/o*IR in blue color) and with IR (CABB-*w*IR in red color) exposure on FTO substrates.

0.191°, respectively, suggesting a highly crystalline form of $Cs_2AgBiBr_6$ HDP crystals. In contrast, CABB-*w/o*IR consistently exhibits a polycrystalline nature regardless of the number of coating layers. To evaluate the single crystalline nature, rocking curve measurements were performed (Fig. S2). The CABB-*w*IR film exhibits the rocking curve peak centered at $\omega = 15.74°$ with an FWHM of 1.18°, indicating a strongly textured/preferential orientation films comprised of porous-SCs. On the contrary, CABB-*w/o*IR films do not show any orientation as the signals from these are too feeble to be detected in this mode.

Raman spectra obtained from CABB-*w*IR and CABB-*w/o*IR thin films show vibrational peaks, including the three strong modes from F_{2g} (~75 $cm^{[-1}$), E_g (~134 $cm^{[-1}$), and A_{1g} (~179 $cm^{[-1}$) (Fig. 1c), characteristics of the $Cs_2AgBiBr_6$ phase[16]. The prominent presence of A_{1g} modes in the Raman spectra distinctly confirms the formation of the $Cs_2AgBiBr_6$ phase[16]. UV-vis absorption and photoluminescence spectra from these thin films also exhibit characteristic features corresponding to phase-pure $Cs_2AgBiBr_6$ [Fig. S3(a, b)]. The CABB-*w*IR thin films exhibit two absorption peaks at ~ 450 and ~ 600 nm with the corresponding estimated direct and indirect bandgap values of 1.76 eV and 2.17 eV from the band edges. These values are similar to that reported for single crystalline quality films[12,13]. Whereas CABB-*w/o*IR films show only one prominent absorption peak at ~ 450 nm. Both the samples exhibit similar PL spectra which is characteristics of self-trapped excitonic emission in CABB[13].

The SEM image in Fig. 2 illustrates the CABB-*w*IR film coated after the first and second layers. Notably, following the initial layer coating, small porous $Cs_2AgBiBr_6$ particle cluster formation with platelets (~ 150 nm thickness) exhibiting specific crystallographic orientation growing in a crisscross manner are observed [Fig. 2(a, b)]. These crystallographic low energy planes in $Cs_2AgBiBr_6$ foster the development of porous-SC clusters composed of platelets ranging in size from 5 to 10 µm, displaying a narrow size distribution (Fig. S4a). Figure 2b showcases an individual porous-SC particle comprised of four vertically aligned platelets of $Cs_2AgBiBr_6$ HDP, as observed from [$\bar{1}01$] direction. The angle between the intersecting platelets indicates their correspondence to { $\bar{1}0\bar{1}$} and {$1\bar{4}1$} planes, and the crystallographic orientation relationship can be easily discerned from the crystal structure illustration provided in Fig. 2c. The size of these clusters may decrease slightly when the temperature is reduced, with the platelet cluster sizes ranging from 3 to 5 µm, as shown in Fig. S5 (a, b). Nonetheless, the growth of specific planes in platelet form remains consistent, suggesting that the solvent evaporation due to temperature variations during deposition may regulate the size of these initial clusters. Consequently, each of these clusters gives rise to single crystalline particles with substantial voids between the platelets. Thus, the gaps between the platelet particles create the pore regions. Additionally, we successfully achieved highly interconnected porous-SC clusters of platelets with uniform distribution and continuity over a large area by dropping the precursor solution over the hot FTO substrate and gently wiping the surface with another heated FTO substrate (Fig.

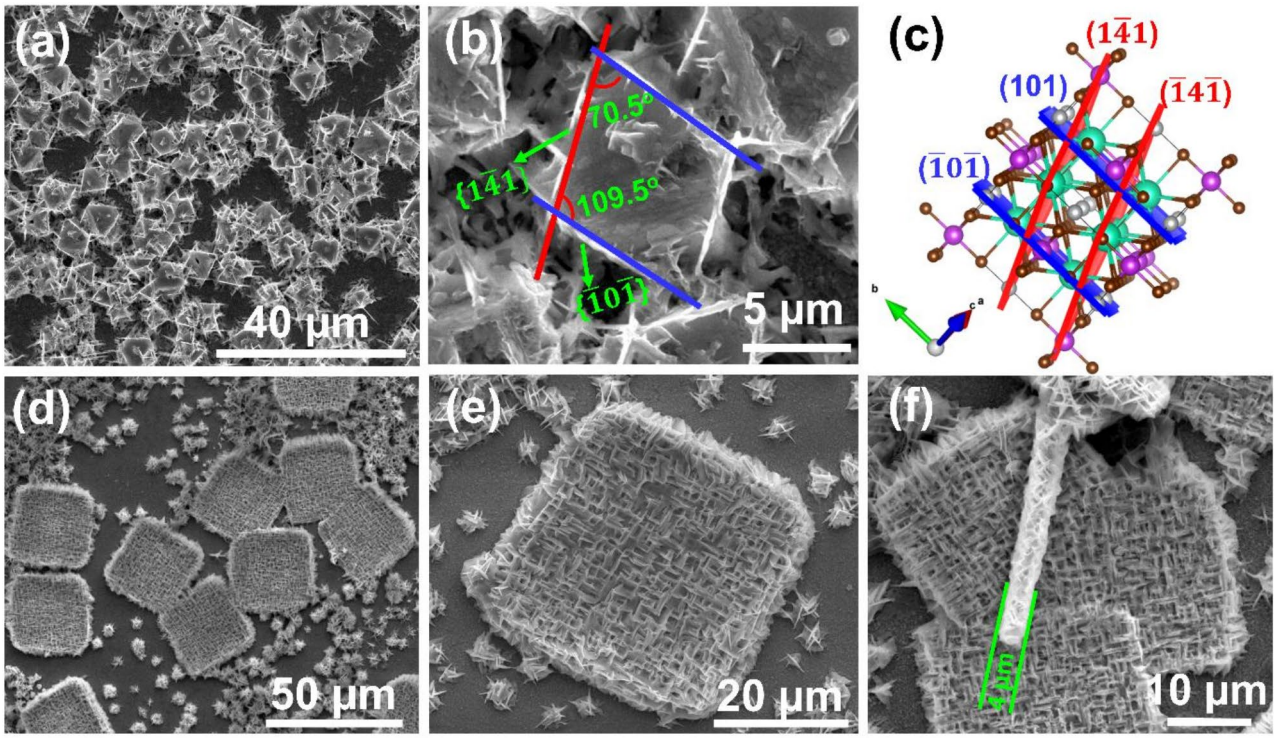

Fig. 2. FESEM images of CABB-*w*IR HDP: (**a**, **b**) Images obtained after the first layer of coating at different magnifications. The blue and red lines in (**b**) depict the orientation of platelets in a single porous particle with platelets originating from crystal facets from { $\bar{1}0\bar{1}$} and {$1\bar{4}1$} planes, as illustrated in (**c**). (**d**, **e**) CABB-*w*IR HDP after two layers of coating. (**e**) Represents a high-magnification SEM image from (**d**). (**f**) The crystal edge of porous-SC looks like the stacking-of-cards.

S6b), under IR illumination. On the other hand, CABB films without IR illumination (CABB-*w/o*IR) obtained by the wiping method do not exhibit any of the platelets features and hence the porous nature exhibited by the interconnected platelet morphology (Fig. S6a).

Upon spin-coating multiple layers with consistent deposition parameters, the smaller porous-SC clusters undergo further growth and transform into significantly larger square-shaped $Cs_2AgBiBr_6$ porous-SCs [Fig. 2(d, e) and supplementary Fig. S5 (c, d)]. The growth of these large $Cs_2AgBiBr_6$ porous-SCs, ranging in size from 10 to 50 µm, is facilitated by the initially distributed smaller porous particles, which serve as seeds for subsequent crystal growth. Smaller porous clusters of crystallographically oriented platelet particles (~ 3–10 µm) present during the initial layer coating merge through appropriate reorientation, aided by the dissolution and agglomeration driven by preferential orientation. This growth process resembles non-classical crystallization[17], wherein oriented platelet particles fuse to form iso-oriented building blocks, eventually leading to the growth of large porous square-shaped $Cs_2AgBiBr_6$ HDP single crystals, with an area ranging from 300 to 900 μm^2 (Fig. 2e and Fig. S4b). The average lateral size of these square-shaped mesoporous $Cs_2AgBiBr_6$ microcrystals is ~ 25 µm. The areal distribution graph for these microcrystals is illustrated in the histogram provided in supplementary Fig. S4b. Typically, these porous-SCs possess a thickness of a few µm as seen from the vertically standing crystal exhibiting ~ 4 µm thickness as shown in Fig. 2f. Furthermore, FESEM imaging of the crystal edge demonstrates that preferentially oriented platelets having a thickness of ~ 150 nm are arranged in a crisscross manner, resembling the stacking-of-cards (Fig. 2f). The porous regions within these crystals result from solvent evaporation aided by the IR light exposure and the rapid growth of preferential crystallographic planes into large platelets. Most importantly, IR lamp exposure, the local temperature of the precursor solution being spin-coated on the substrate plays a pivotal role in accelerating solvent evaporation, thereby facilitating the further growth of smaller porous particles into larger porous microcrystals. The absorption of IR light by the solvent and/or FTO substrate, the resultant local heat, the evaporation rate of solvent associated with a local super saturation and nucleation, and the rapid growth of low energy crystallographic facets of CABB, all leads to this fascinating porous-SC growth (shown in schematic illustration Fig. S7). To further clarify the role of local heating effect, experiments were conducted under white LED (higher energy visible) light illumination. We could not find any evidence for the porous-SC formation as shown in Fig. S8. After the first layer coating, particles with intertwined cubic morphology are predominantly formed, and after second layer coating a fully-grown octahedral morphology evolves. In the absence of local heating, which is the case with the visible light, these crystals grow naturally, as the solvents evaporate at much slower rate. Thus, it is evident that the IR absorbed by the solvent and/or FTO leading to the local heating and evaporation, is what most important factor in the formation of porous-SC of CABB.

The concentration precursor solution is also important as the porous crystals are formed only at higher concentration (~ 1.2 mmol) in the solvent (Fig. S9 & S10). If the solvent temperature is elevated, either by increasing the substrate temperature or by moving the IR lamp closer to the substrate, the crystal may melt and lose the sharp faceted platelets, transforming into continuously connected nanoparticles, while still retaining the overall square shape of the micron-sized crystal. Supplementary Fig. S11(a-c) depicts such a scenario where facetted nanoplatelets lose the porous texture when deposited at a higher temperature ($T > 100$ ℃). Notably, films grown without IR light illumination (CABB-*w/o*IR) do not exhibit any porous microstructure (Fig. S12). The porous-SC demonstrate compositional uniformity, maintaining the expected 2:1:1:6 ratios for Cs, Ag, Bi and Br (Fig. S13).

To further elucidate the single-crystal nature of the porous crystal, we performed angle-resolved polarized Raman spectroscopy for both CABB-*w*IR and CABB-*w/o*IR films (Fig. 3(a-b) and S14). Raman intensity of the prominent modes was monitored while rotating the incident laser (~ 5 µm spot size) polarization direction by adjusting the half-wave plate (azimuthal angle φ′ as shown in Fig. 3a & S14a). To better illustrate the variation in intensity as a function φ′, the polar plots of F_{2g}, E_g, and A_{1g} modes of the CABB-*w*IR and CABB-*w/o*IR films are plotted as shown in Fig. 3b and Fig. S14b, respectively. In CABB-*w*IR film the intensity of the F_{2g} and A_{1g} modes (E_g mode) reaches maximum (minimum) when the analyzer and the polarizer are aligned parallel to one of the crystal edges (i.e., at φ′ ~ 20°), and minimum (maximum) when the incident polarization is perpendicular to the analyzer. This two-fold anisotropic behavior of vibrational modes confirms the single-crystal nature of the $Cs_2AgBiBr_6$ porous-SC and notably such as behavior is not observed in CABB-*w/o*IR (Fig. S14). This strong evidence that IR assisted grown porous CABB microstructure is a single crystal is also substantiated by the spot pattern noted from the single crystal diffraction pattern taken from a single square-shaped CABB-IR porous-SC (Fig. S15). Raman mapping images based on the intensity of E_g and A_{1g} modes of a CABB-*w*IR porous-SCs indicate that the crystal exhibits phase and compositional homogeneity (Fig. S16). Additionally, the porous $Cs_2AgBiBr_6$ HDP was examined using transmission electron microscopy to analyze its single crystalline nature. Given the considerable thickness of the crystals, we captured the images from the edge of the particles. A representative bright-field image of mesoporous $Cs_2AgBiBr_6$ is shown in Fig. 3c. The selected area electron diffraction image taken from this region exhibits an ordered spot pattern indicating a single crystalline nature (Fig. 3d). The pattern corresponds to a cubic structure, with the diffraction spots indexed to the plane from the zone axis $[10\ \bar{1}\ 1]$.

Solar cell device performance

To harness the advantage of the porous nature of $Cs_2AgBiBr_6$ films, we investigated the photovoltaic performance by fabricating *n-i-p* heterojunction solar cell devices (see Fig. S17 in SI files). Photovoltaic devices using polycrystalline non-porous (PC-nP) (CABB-*w/o*IR) and porous SC (CABB–*w*IR) thin films were fabricated under similar conditions with the solar cells active area of 3.14 mm^2. The cross-sectional SEM image of the CABB-*w*IR coated on m-TiO_2/c-TiO_2/FTO/Glass substrate is shown in Fig. 4a. Current density vs. voltage (J-

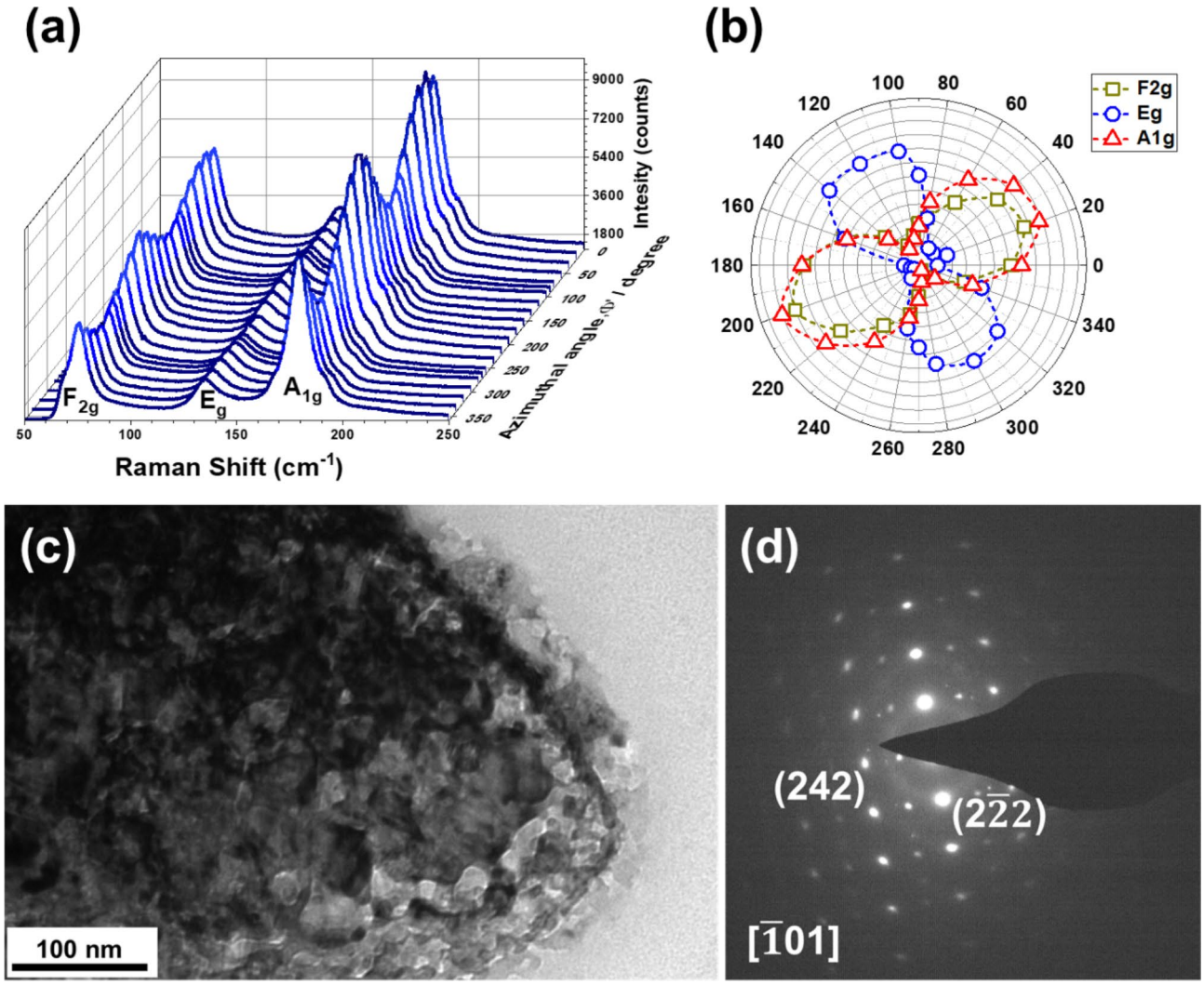

Fig. 3. (**a**) Raman spectra obtained under crossed polarization from a porous-SC $Cs_2AgBiBr_6$ HDP for different azimuthal rotation angles ϕ′. (**b**) Polar plot of the integrated Raman intensity of the F_{2g}, E_g, A_{1g} modes of a porous-SC $Cs_2AgBiBr_6$ HDP. (**c**) Bright-field TEM image and (**d**) Selected area electron diffraction taken from a mesoporous crystal, matching with the [10 $\bar{1}$] zone axis of a cubic $Cs_2AgBiBr_6$.

V) curves of a representative best cell prepared from the porous-SC $Cs_2AgBiBr_6$ device are shown in Fig. 4(b). For comparison, the best performance of a cell fabricated with the PC-nP layer of CABB-*w/o*IR is also shown. The observed short-circuit current density (J_{SC}) and open-circuit voltage (V_{OC}) of the porous-SC $Cs_2AgBiBr_6$ perovskite solar cell device are 1.40 mA/cm^2 and 1.04 V, respectively. In contrast, for a device made with a conventional planar CABB-*w/o*IR perovskite thin film layer, the J_{SC} value is small (0.55 mA/cm^2), while the V_{OC} is nearly the same, 0.94 V. The porous nature of the $Cs_2AgBiBr_6$ perovskite crystals significantly enhances the J_{SC} by more than twice compared to the PC-np CABB-*w/o*IR thin film device. This improved J_{SC} is attributed to the large surface area and scattering effects resulting from the porous nature of the perovskite film. From the optical absorption spectra (Fig. S3) also we could see that the CABB-*w*IR shows higher absorbance than the CABB-*w/o*IR film. This may result from the scattering effect in the porous morphology of CABB-SC. The crisscross textured surface in CABB porous-SC causes light to scatter, directing more light into the active layer and effectively increasing the optical path length of incident light within the perovskite layer. Hence, enhanced light absorption seen in absorption spectra also strongly implies the increased J_{SC}. The photovoltaic power conversion efficiency of porous-SC and polycrystalline non-porous $Cs_2AgBiBr_6$ devices is 0.86% and 0.28%, respectively. It should be noted that slightly lower values observed in our devices are due to the films prepared in air ambient without any use of antisolvent or any other assisted method and tested them in open air ambient after spin coating the HTL (Spiro-OMeTAD) in the Ar glove box. Although these values are slightly lower than the reported CABB devices, most of the report had utilized specific conditions like the active layer preparation process including antisolvent (chlorobenzene (CB), isopropyl alcohol (IPA)) assisted, low pressure assisted, hydrogenation treatment, DMSO and DMF mixture, ionic liquids, solvent vapour assisted, layer by layer deposition and gas quenching approach to improve the solar cell efficiency (see the Table S1 in the supplementary section). The change in the J_{SC} and

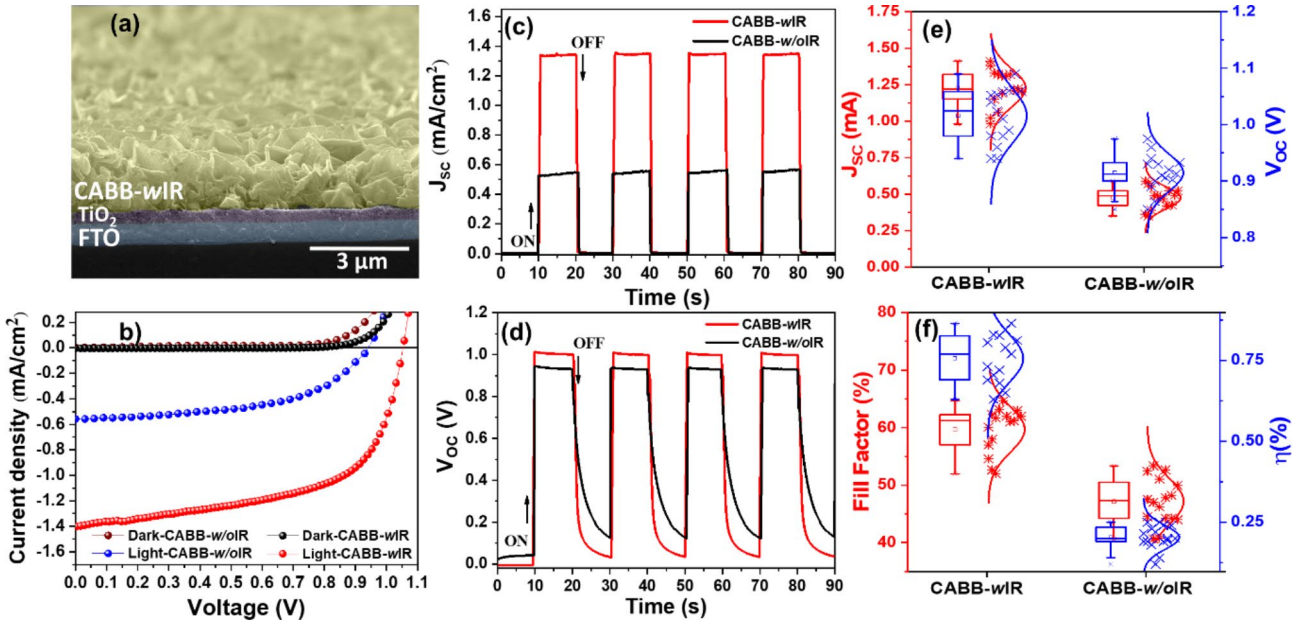

Fig. 4. (**a**) Cross-sectional SEM image of FTO/c-TiO_2/m-TiO_2/ CABB–*w*IR. (**b**) The plot of current density (J) versus voltage (V) for champion cells made utilizing CABB-*w*IR and CABB-*w/o*IR. (**c**) and (**d**) show the variation of short circuit current (J_{SC}) and voltage (V_{OC}) versus time, respectively, under light ON and OFF conditions, (**e**), and (**f**) depict statistical distribution graphs of photovoltaic parameters, including J_{SC}, V_{OC}, FF, and efficiency (η%) for devices made utilizing CABB-*w*IR and CABB-*w/o*IR films.

V_{OC} for the porous-SC and PC-nP CABB-*w/o*IR perovskite films as a function of time under the ON and OFF conditions of AM 1.5 source light is presented in Fig. 4(c) and (d). The J_{SC} is almost two and a half times higher (J_{SC} =1.40 mA/cm^2) for the device with CABB-*w*IR comprising porous-SCs compared to the PC-nP CABB-*w/o*IR films (J_{SC} = 0.55 mA/cm^2) under light ON conditions. In both devices, the J_{SC} instantaneously becomes zero when the light is turned OFF. V_{OC} is also slightly higher (~ 10%) for CABB-*w*IR compared to the CABB-*w/o*IR films. Several cells fabricated under identical conditions were tested for the J-V photovoltaic performance. The distribution in the photovoltaic parameters, along with the mean and standard deviation is presented in Fig. 4(e) and (f). The photovoltaic parameters demonstrate the advantage of porous-SC CABB-*w*IR films, exhibiting better J_{SC} and V_{OC}, as well as fill-factor values, over the polycrystalline CABB-*w/o*IR films without pores. The porous film accommodates the Spiro-OMeTAD (HTL) layer, hence it facilitates a large interface between the active layer and HTL layer for an efficient extraction of charge carriers. This is akin to the case of a dye-sensitized solar cells, where the dye (photoactive component) is coated on the porous TiO_2 (ETL layer). In our case, the HTL layer gets coated on the open surface available in the porous region of the CABB (Fig. S18). This will effectively reduce the recombination in CABB and reduce trap density (Fig. S19) and hence increase J_{SC}. Since the thickness of the CABB-*w*IR and CABB-*w/o*IR films are almost similar, i.e. 4 µm, there is no role of thickness difference in enhancing the J_{SC} (Fig. S20). Alternatively, the light scattering from the porous region can also contribute to a certain extent to the enhancement of J_{SC}. To prove that we performed the EQE measurements for both samples by illuminating light through the n-side of the device, as shown in Fig. S21. Compared to the CABB-*w/o*IR device, the CABB-*w*IR device demonstrates stronger absorption in the higher wavelength region (375–550 nm) of the spectrum. This enhancement may be attributed to scattering effects, which increase the optical path length within the material, thereby enhancing the probability of absorption. This might contribute to the higher J_{SC} observed in the CABB-*w*IR device. The enhanced PCE in our case indeed supports the fact that the porous nature of the CABB is the prime factor in enhancing the photovoltaic properties, as there are no other factors that would be attributable to the changes in these two devices. The stable power output measurements of the FTO/TiO_2/CABB-*w*IR/Spiro-oMeTAD/Au and FTO/TiO_2/CABB-*w/o*IR/Spiro-oMeTAD/Au devices also suggest the robust nature of the device with the porous CABB (Fig. S22).

Since, the porous nature of the CABB HDP can be utilized in photodetector aspect as well, the responsivity and detectivity of the device were calculated. Responsivity and detectivity values for the CABB-*w*IR are 13 mA/W and 2.08×10^9 Jones, and for CABB-*w/o*IR values are 5.3 mA/W, and 2.2×10^9 Jones, respectively.

This method of obtaining porous-SCs can be extended to other related HDPs. Figure 5 shows the FESEM images of various compositions where either B′ or the B′′ cations in $Cs_2B'B''X_6$ HDPs are changed. Figure S23 shows the detailed structural, microstructural and optical properties of these different compositions. Such variation in HDPs is explored extensively in the literature to tailor the optical properties of these compounds.

Conclusion

In conclusion, our study demonstrates that IR-light-assisted spin coating enables the fabrication of porous single crystals (porous-SCs) of $Cs_2AgBiBr_6$ halide double perovskite. The porous structure arises as the platelets with

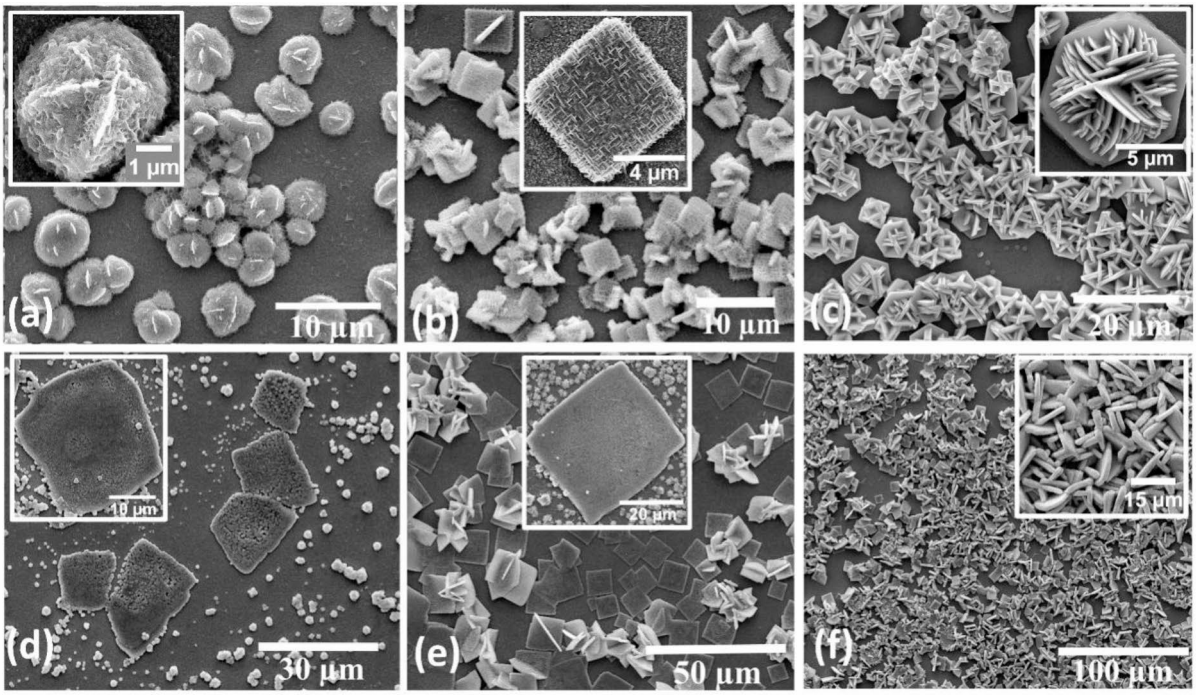

Fig. 5. FESEM images $Cs_2AgBiBr_6$ related HDPs: (**a**) $Cs_2AgBi_{0.6}Sb_{0.4}Br_6$, (**b**) $Cs_2Ag_{0.7}Cu_{0.3}BiBr_6$ (**c**) $Cs_2AgSbBr_6$ (**d**) $Cs_2AgBiCl_6$, (**e**) $Cs_2Ag_{0.9}Cu_{0.1}BiBr_6$, (**f**) $Cs_2AgBi_{0.5}In_{0.5}Br_6$.

specific crystallographic orientation grow in a crisscross manner, fusing to form iso-oriented building blocks akin to a non-classical crystallization process. We achieved square-shaped porous-SCs as large as ~50 µm and with pore sizes ranging from 0.2 µm to 2 µm. Solar-cell devices fabricated with these porous-SCs exhibit enhanced power conversion efficiency compared to conventional polycrystalline films obtained without IR-assisted spin coating. Specifically, the J_{SC} and V_{OC} are ~60% and ~10% higher, respectively, for the porous-SC $Cs_2AgBiBr_6$ perovskite solar cell device compared to the conventional polycrystalline non-porous thin films. The high surface area available in porous-SC effectively facilitates charge separation at the interface between perovskite and ETL/HTL layers. The IR-light-assisted spin coating has been extended to various $Cs_2AgBiBr_6$ related compositions to synthesize them in porous-SC form. Porous single-crystal halides hold promise for various optoelectronic and photoelectrochemical applications.

Supporting information

The experimental procedure, XRD pattern of single-layer coated CABB HDP thin film under IR light illumination, optical absorption and emission spectrum of porous-SC CABB-*w*IR film, histogram of platelet cluster area distribution after single-layer coating and porous-SC area after two layers of spin coating process; FESEM images of CABB-*w*IR HDP at different magnification after 1st the layer of coating, after the 2nd layer of coating, and uniform porous crystal $Cs_2AgBiBr_6$ film under IR illumination; FESEM images of spin-coated $Cs_2AgBiBr_6$ film at $T > 100$ °C, and without IR illumination; X-ray EDS elemental maps of a representative porous-SC CABB-*w*IR HDP; Raman mapping of E_g and A_{1g} vibrational modes for porous-SC $Cs_2AgBiBr_6$-wIR HDP; Solar cell fabrication procedure, the device schematic diagram, the cross-sectional SEM image, and the energy level diagram of the FTO/c-TiO_2/m-TiO_2/ CABB–wIR/Spiro-OMeTAD solar cell.

Data availability

Data is provided within the manuscript or supplementary information files.

Received: 2 September 2024; Accepted: 1 January 2025
Published online: 04 January 2025

References

1. Li, W. & Xie, K. Porous single crystals at the Macroscale: from growth to application. *Acc. Chem. Res.* **56**, 374–384 (2023).
2. Zhang, F. et al. Metallic Porous Iron Nitride and Tantalum Nitride single crystals with enhanced Electrocatalysis Performance. *Adv. Mater.* **31**, (2019).
3. Crossland, E. J. W. et al. Mesoporous TiO_2 single crystals delivering enhanced mobility and optoelectronic device performance. *Nature* **495**, 215–219 (2013).
4. Lin, G., Xi, S., Pan, C., Lin, W. & Xie, K. Growth of 2 cm metallic porous TiN single crystals. *Mater. Horizons*. **5**, 953–960 (2018).

5. Xiao, Y., Li, H. & Xie, K. Activating Lattice Oxygen at the twisted surface in a mesoporous CeO_2 single crystal for efficient and Durable Catalytic CO Oxidation. *Angew Chemie - Int. Ed.* **60**, 5240–5244 (2021).
6. Yu, X., Cheng, F., Duan, X. & Xie, K. Porous Single-Crystalline Monolith to Enhance Catalytic Activity and Stability. *Research* (2022). (2022).
7. Li, X. & Xie, K. Porous single-crystalline molybdenum nitride enhances electroreduction of nitrogen to ammonia. *Front. Mater.* **9**, 1–9 (2022).
8. Zhang, Z. et al. Hydrogenated $Cs_2AgBiBr_6$ for significantly improved efficiency of lead-free inorganic double perovskite solar cell. *Nat. Commun.* **13**, 3397 (2022).
9. Jagadeeswararao, M. et al. Stoichiometric Engineering of $Cs_2AgBiBr_6$ for photomultiplication-type photodetectors. *Chem. Mater.* **35**, 3095–3104 (2023).
10. Prabhu, K. & Chandiran, A. K. Solar energy storage in a $Cs_2AgBiBr_6$ halide double perovskite photoelectrochemical cell. *Chem. Commun.* **56**, 7329–7332 (2020).
11. Ye, H. et al. Optoelectronic Resistive Memory based on lead-free $Cs_2AgBiBr_6$ double perovskite for Artificial Self-Storage Visual Sensors. *Adv. Electron. Mater.* **9**, (2023).
12. Gao, W. et al. High-Quality $Cs_2AgBiBr_6$ Double Perovskite Film for Lead-Free Inverted Planar Heterojunction Solar Cells with 2.2% Efficiency. *ChemPhysChem* 19, 1696–1700 (2018).
13. Slavney, A. H., Hu, T., Lindenberg, A. M. & Karunadasa, H. I. A Bismuth-Halide double perovskite with long carrier recombination lifetime for photovoltaic applications. *J. Am. Chem. Soc.* **138**, 2138–2141 (2016).
14. McClure, E. T., Ball, M. R., Windl, W. & Woodward, P. M. Cs_2AgBiX_6 (X = br, cl): new visible light absorbing, lead-free Halide Perovskite Semiconductors. *Chem. Mater.* **28**, 1348–1354 (2016).
15. Hoye, R. L. Z. et al. Fundamental carrier lifetime exceeding 1 µs in $Cs_2AgBiBr_6$ double perovskite. *Adv. Mater. Interfaces* **5**, (2018).
16. Dakshinamurthy, A. C., Gupta, M., Nanda, B. R. K. & Sudakar, C. Anionic Alloying in Hybrid Halide $Cs_2AgBiBr_{6-x}Cl_x$ double perovskites: is it true alloying or Preferential Occupation of Halide ions in MX 6 Octahedra? *J. Phys. Chem. C.* **127**, 1588–1597 (2023).
17. Vasanth Kumar, K. et al. Nonclassical crystal growth and growth rate hysteresis observed during the growth of curcumin in impure solutions. *CrystEngComm* **25**, 3361–3379 (2023).

Acknowledgements

C.S. acknowledges the support by DST-SERB for funding this work through the SUPRA grant vide SPR/2021/000499. C.S. acknowledges the support by MoE, India, through the Institutes of Eminence (Grant No. SP20210777DRMHRDDIRIIT) for the research initiatives on establishing the Research Centre for Advanced Microscopy and Materials (Grant No. SB20210844MMMHRD008277). The authors acknowledge the help from Swapneswar Bisoi, and Debnath Samanta for coating TiO_2 layers on FTO, preparation precursor solution, and spin coating.

Author contributions

C.S. and M.S.P proposed and designed the project. M.S.P and A.K performed all the experiments, A.K fabricated and tested the solar cell devices, S.G did the TEM studies. All the authors analyzed the data and wrote the paper.

Declarations

Competing interests

The authors declare no competing interests.

Additional information

Supplementary Information The online version contains supplementary material available at https://doi.org/10.1038/s41598-025-85326-2.

Correspondence and requests for materials should be addressed to C.S.

Reprints and permissions information is available at www.nature.com/reprints.

Publisher's note Springer Nature remains neutral with regard to jurisdictional claims in published maps and institutional affiliations.